

Kinetic-Rotor Self-Commissioning of Synchronous Machines for Magnetic Model Identification with Online Adaptation

*Original*

Kinetic-Rotor Self-Commissioning of Synchronous Machines for Magnetic Model Identification with Online Adaptation / Varatharajan, A.; Pellegrino, G.; Armando, E.. - In: IEEE TRANSACTIONS ON INDUSTRY APPLICATIONS. - ISSN 0093-9994. - ELETTRONICO. - (2022), pp. 1-1. [10.1109/TIA.2022.3151039]

*Availability:*

This version is available at: 11583/2956404 since: 2022-02-25T10:44:58Z

*Publisher:*

Institute of Electrical and Electronics Engineers Inc.

*Published*

DOI:10.1109/TIA.2022.3151039

*Terms of use:*

This article is made available under terms and conditions as specified in the corresponding bibliographic description in the repository

*Publisher copyright*

IEEE postprint/Author's Accepted Manuscript

©2022 IEEE. Personal use of this material is permitted. Permission from IEEE must be obtained for all other uses, in any current or future media, including reprinting/republishing this material for advertising or promotional purposes, creating new collecting works, for resale or lists, or reuse of any copyrighted component of this work in other works.

(Article begins on next page)



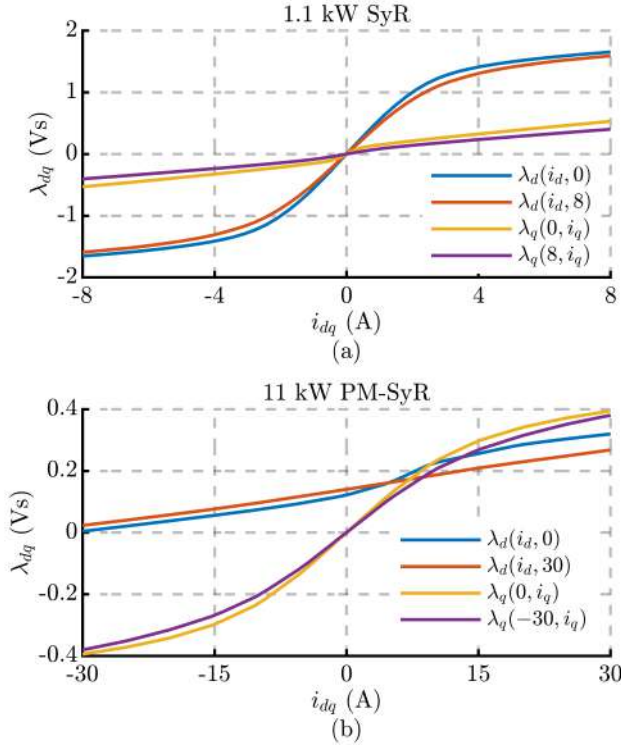


Fig. 2. Experimentally obtained flux-map of the two motors under test identified with the constant speed test [4]: (a) 1.1 kW SyR motor; (b) 11 kW PM-SyR motor.

speed regulation is achieved by varying the duty-cycle of the bipolar  $i_q$  through a low-frequency pulse-width-modulation (LF-PWM) structure. A speed hysteresis control is used in [7] where the frequency of speed reversal is determined by the torque at a given operating point (and the shaft inertia). In turn, a higher mechanical noise was observed at higher speed reversal frequencies for the machine under test. This prompted the need for improvement/development of the LF-PWM scheme for speed regulation. The inability of [7] to characterize the self-saturation curves due to the zero-torque areas is fixed in this new technique. Besides a position encoder, neither a dedicated rig nor any additional hardware is necessary. Respect to [13], the proposed method characterizes the cross-saturation phenomenon with precision, although with the help of an encoder. As many synchronous machines are not innately provided with a position encoder, the proposed technique is also applicable as an end-of-line MMI, where the motor under test is coupled to an external encoder and identified within a few minutes, without the use of a prime mover or data recorders.

The projection vector framework is introduced in [15], [16] in the context of sensorless control where the discrepancy between the observed and the current-model flux estimates is used for position estimation. A similar framework is exploited in this work for populating the flux-map LUTs via flux adaptation, under measured rotor position conditions. The stator resistance is also adaptively compensated within the same framework. While the proposed scheme is validated on a SyR machine in the conference work [17], this paper

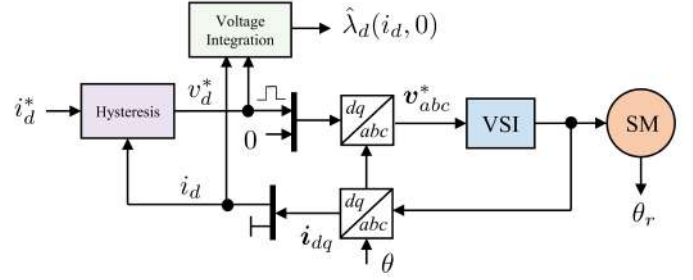


Fig. 3. Self-saturation identification test-d at standstill: hysteresis current controller in  $d$ -axis with square-wave voltage injection and direct voltage integration.

shows the feasibility on a PM-SyR machine, making the self-commissioning technique applicable to the entire family of synchronous machines (including synchronous wound-field machines).

The main features of this work are enumerated as follows:

- 1) Low-frequency modulated current references is proposed for speed regulation at free-shaft to systematically explore the  $dq$  current plane.
- 2) The speed region of operation is optimized for a reliable flux estimation in the shortest time. The frequency of speed rate reversal is calibrated to limit the mechanical vibrations.
- 3) An online stator flux adaptation scheme is devised using the projection vector framework that makes the post-processing stage obsolete.
- 4) Furthermore, a stator resistance adaptation is developed that tracks the temperature-induced variations of the resistance and the non-ideal inverter dead-time compensation.

The proposed control scheme for the magnetic model identification with self-acceleration and deceleration is discussed in Section II and the online adaptation using the projection vector framework is elaborated in Section III. Section IV reports the experimental validation on a 1.1 kW SyR and a 11 kW PM-SyR motors. Section V concludes the paper.

## II. PROPOSED CONTROL SCHEME FOR MMI

The electrical rotor position is  $\theta$  and the electrical angular speed is  $\omega = s\theta$  where  $s$  is the differential operator  $\frac{d}{dt}$ . Estimated vectors are represented by the superscript  $\hat{\cdot}$ . The orthogonal rotational matrix is  $\mathbf{J} = \begin{bmatrix} 0 & -1 \\ 1 & 0 \end{bmatrix}$  and  $\mathbf{I}$  is the identity matrix. Real space vectors will be used; for example, the stator current is  $\mathbf{i}_{dq} = [i_d, i_q]^T$  where  $i_d$  and  $i_q$  are the vector components in rotor reference frame. Space vectors in the stationary reference frame are denoted by subscript  $\alpha\beta$ .

The convention for a SyR machine is that the  $d$ -axis is aligned with the maximum inductance path, i.e., motoring and braking for positive speeds occurs in the first and the fourth quadrant, respectively. For the machines with magnets, the  $d$ -axis is aligned with the magnet such that motoring and braking occurs in the second and the third quadrant, respectively.

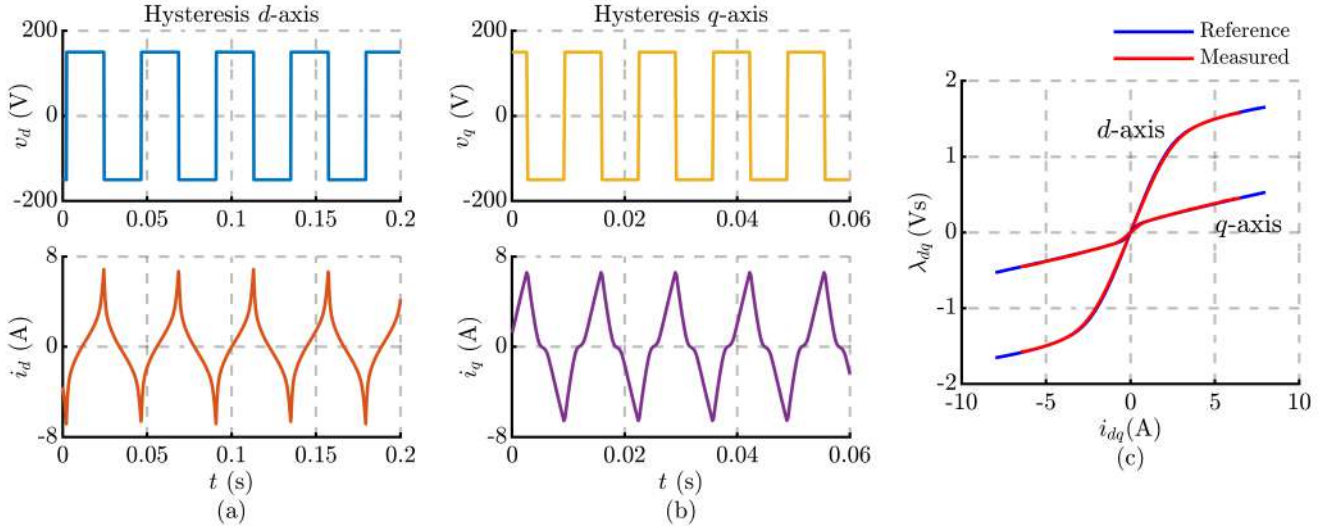


Fig. 4. SyR machine self-saturation identification: time plots of hysteresis controller (a) Test- $d$  and (b) Test- $q$ ; (c) Validation with the reference curves.

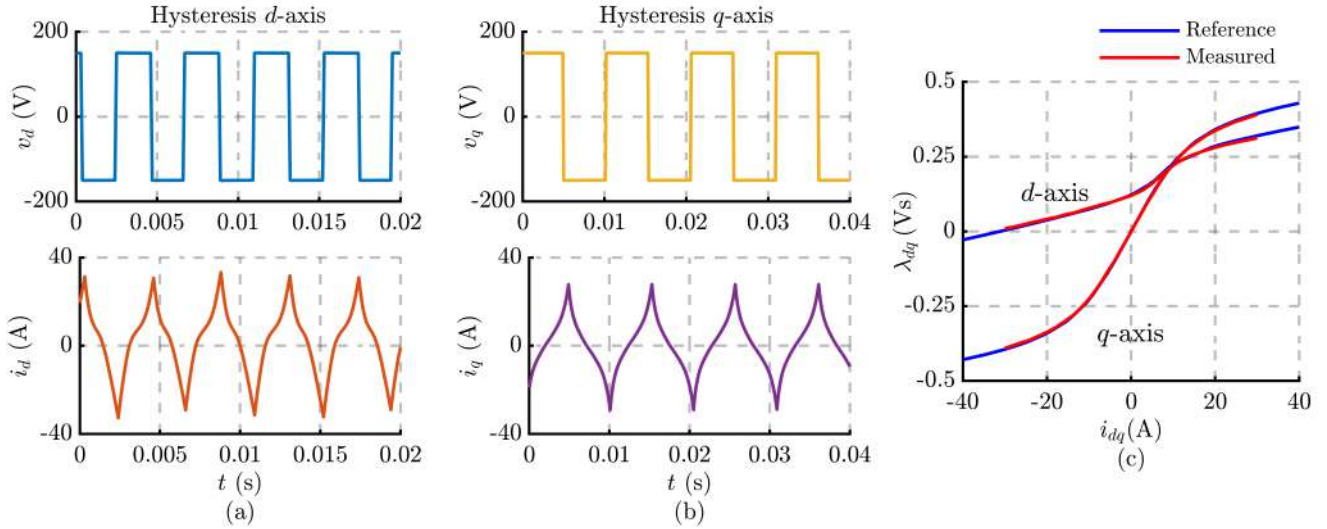


Fig. 5. PM-SyR machine self-saturation identification: time plots of hysteresis controller (a) Test- $d$  and (b) Test- $q$ ; (c) Validation with the reference curves.

#### A. Synchronous Machine Model

The voltage equation of a synchronous machine in the rotor reference frame can be expressed as

$$s \lambda_{dq} = v_{dq} - R_s i_{dq} - \omega \mathbf{J} \lambda_{dq} \quad (1)$$

where  $R_s$  is the stator resistance and  $\lambda_{dq}$  is the stator flux linkage. The time derivative of the stator flux can be expressed with the incremental inductance matrix  $\mathbf{L}_\partial$  as

$$\mathbf{L}_\partial = \frac{\partial \lambda_{dq}}{\partial i_{dq}} = \begin{bmatrix} l_d & l_{dq} \\ l_{dq} & l_q \end{bmatrix} \quad (2)$$

where  $l_d, l_q$  represents the incremental inductance along direct  $d$  and quadrature  $q$  axis, respectively, while  $l_{dq}$  is the cross-saturation term. All quantities are functions of  $i_{dq}$ . The average electromagnetic torque is given by

$$T = \frac{3p}{2} i_{dq}^T \mathbf{J} \lambda_{dq} \quad (3)$$

where  $p$  is the number of pole pairs.

The reference flux-map of the two motors under test are experimentally identified using the three-pulse constant speed test [4] and are shown in Fig. 2, illustrating the saturation and cross-saturation properties. The proposed magnetic model identification is comprised of two stages: i) test- $d$  and test- $q$  for self-saturation identification,  $\lambda_d(i_d, 0)$  and  $\lambda_q(0, i_q)$ , respectively; ii) test- $dq$  for cross-saturation identification.

#### B. Hysteresis Control for Self-Saturation Identification

The  $dq$  operating points on the zero-torque locus are incapable of self-acceleration and deceleration. Thus, they are identified with a hysteresis controlled square-wave voltage injection at standstill, as shown in Fig. 3, where the magnetic model of  $d$ -axis is identified without cross-saturation ( $i_q = 0$ ), referred as test- $d$  (test  $i$  in [13]). Similar exploration of  $q$ -axis with hysteresis square-wave voltage injection at  $i_d = 0$  is referred as test- $q$  (test  $ii$  in [13]).



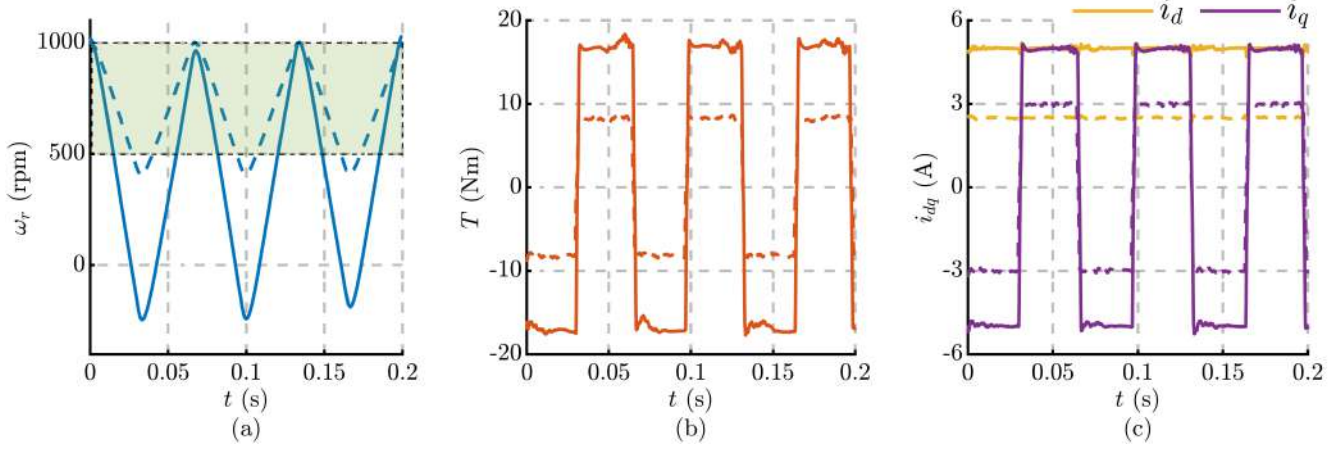


Fig. 6. SyR machine experimental time plots of cross-saturation identification: (a) Mechanical speed where the shaded region represents the optimal speed span for online adaptation; (b) Bipolar torque estimate; (c) Constant  $d$  and bipolar  $q$ -axis currents. Line Marker: dotted lines denote identification at  $i_d^* = 2.5$  A &  $|i_q^*| = 3$  A; continuous lines denote identification at  $i_d^* = 5$  &  $|i_q^*| = 5$  A.

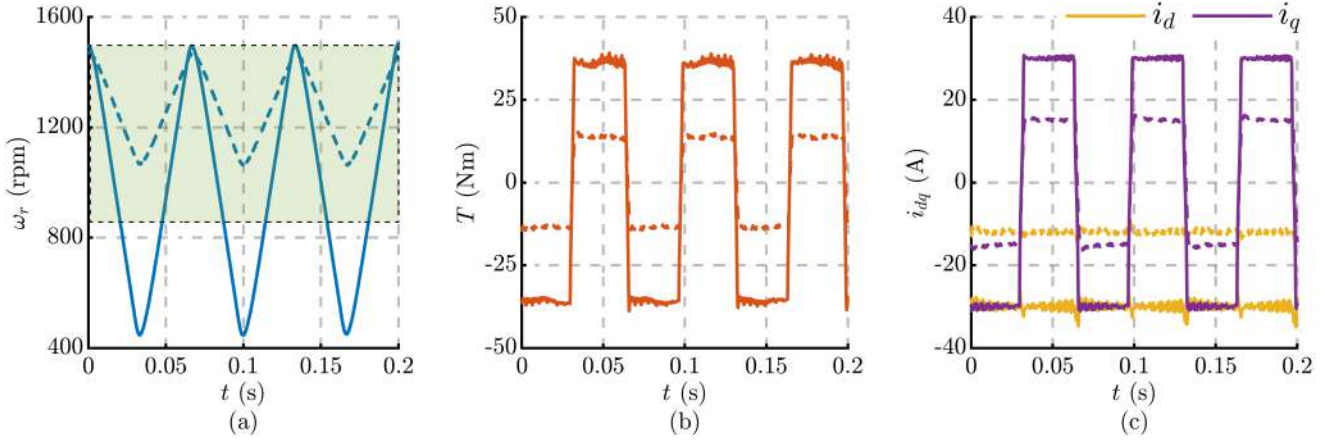


Fig. 7. PM-SyR machine experimental time plots of cross-saturation identification: (a) Mechanical speed where the shaded region represents the optimal speed span for online adaptation; (b) Bipolar torque estimate; (c) Constant  $d$  and bipolar  $q$ -axis currents. Line Marker: dotted lines denote identification at  $i_d^* = -15$  A &  $|i_q^*| = 18$  A; continuous lines denote identification at  $i_d^* = -30$  A &  $|i_q^*| = 30$  A.

The time-plots of test- $d$  and test- $q$  on the SyR machine is shown in Fig. 4(a) and 4(b), respectively. Due to the smaller inductance in the  $q$ -axis, a higher hysteresis frequency is observed. The square-wave voltage magnitude is set to 150 V (0.46 p.u.) and the current is limited to twice the rated value,  $i_d^* = i_q^* = 6.5$  A (2 p.u.). The stator flux is computed from the integration of voltage equation (1), shown in Fig. 4(c) where a good correlation with the reference curves is discerned. This initial self-saturation look-up tables  $\lambda_d(i_d, 0)$ ,  $\lambda_d(0, i_q)$  are stored in the flux-map LUTs of the flux observer  $\hat{\Lambda}_d$ ,  $\hat{\Lambda}_q$ , where the superscript  $\hat{\cdot}$  stands for the *estimated* nature of the LUTs.

Similar results on the PM-SyR machine is shown in Fig. 5. Note that for machines with magnets, test- $q$  is not strictly necessary as it is not a zero-torque locus unlike the SyR machines. Nevertheless, test- $q$  is feasible as the high hysteresis frequency ensures fast torque reversals, maintaining standstill condition. The permanent magnet flux amplitude is estimated from the back-emf at high speeds. For the sake of uniformity,

Fig. 5 reports the results of both test- $d$  and test- $q$  where a good correlation with the reference curves is observed.

### C. LF-PWM Scheme for Cross-Saturation Identification

The identification of cross-saturation requires the exploration of the  $dq$  current plane. However, a non-zero  $|i_q^*|$  (and a non-zero  $|i_d^*|$  for a SyR machine) generates electromagnetic torque and results in rotor movement. In the absence of a driving machine, the machine under identification should be capable of self-regulating the speed and at the same time, systematically explore the torque producing operating points.

To this end, the control technique developed for cross-saturation identification at free-shaft, shown in Fig. 1, is the new contribution of this work. The speed regulation for a given  $i_{dq}^*$  data point is achieved by imposed a constant  $d$ -axis current  $i_d = i_d^*$  and a bipolar  $q$ -axis current  $i_q = \pm|i_q^*|$  for  $q$ -axis current is used for alternating self-acceleration and deceleration around the speed set-point, as shown in Fig. 6 for the SyR machine and Fig. 7 for the PM-SyR machine. The

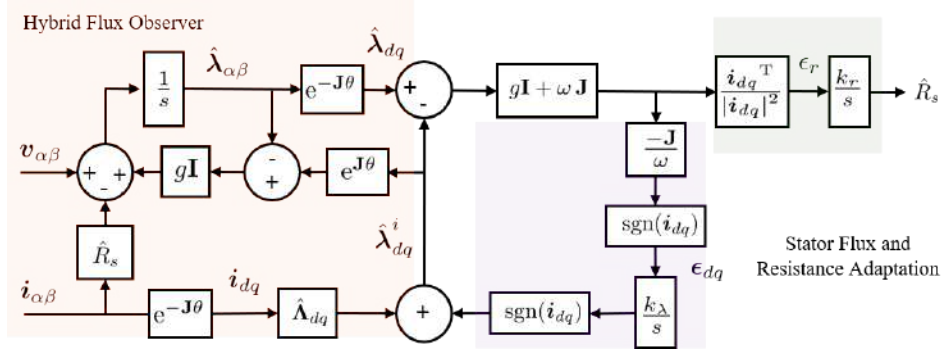


Fig. 8. Proposed scheme of hybrid flux observer with online current-model flux and stator resistance adaptation for cross-saturation identification.

speed controller establishes an average speed equal to the reference speed by imposing an average  $q$ -axis current reference  $i_{q,avg}$ . A low frequency pulse-width-modulation (LF-PWM) is used to calibrate the duty cycle of the bipolar  $i_q^*$  reference such that the mean value respects the speed controller commanded  $i_{q,avg}$ . The frequency of modulation  $f_q$  for LF-PWM should be an order higher than the bandwidth of speed controller. Note that the LF-PWM is not to be confused with the PWM inverter gate signals for the reference voltage realization. The closed-loop speed control is implemented with CVC scheme to impose reference current  $i_{dq}^*$  and the parameters from the self-saturation test can be used to tune the CVC regulators.

Around nominal speed, iron losses gains significance whereas at very low speeds, flux estimation is unreliable due to the low signal-to-noise (SNR) of the back-emf signal integral. Hence, the mechanical speed span  $0.33 < |\omega_r| < 0.66$  p.u. is considered optimal for MMI, represented by the shaded region in Figs.6(a) and 7(a). Ideally, it is desirable to confine the operation within optimal speed span by adapting the LF-PWM modulation frequency  $f_q$  as a function of the torque. However, this is not feasible due to the excessive mechanical vibrations for high  $f_q$  at high torque operating points. Alternatively, the maximum speed and the LF-PWM frequency  $f_q$  are held constant at 0.66 p.u and 15 Hz (experimentally calibrated), respectively, while the lower speed limit (speed-span) varies according to the torque. To this end, the speed reference is determined as

$$\omega^* = (\omega_n \times 0.66) - \frac{\omega_{span}}{2} \quad (4)$$

where  $\omega_n$  is the rated angular speed and  $\omega_{span}$  is the speed-span computed online from the maximum and minimum speed in a LF-PWM cycle. It must be noted that only the data points at steady-state currents within the optimal speed span are engaged in online adaptation, as discussed in the following. The self-saturation LUTs will be corrected for cross-saturation using an hybrid flux observer and a flux adaptation technique mutated from sensorless control, as described in the next section.

### III. PROJECTION VECTOR FRAMEWORK FOR ONLINE ADAPTATION

The block diagram of proposed scheme with hybrid flux observer for online stator flux and resistance adaptation is

shown in Fig. 8.

#### A. Hybrid Flux Observer

The state equation of the flux observer in stator reference frame is defined as

$$s\hat{\lambda}_{\alpha\beta} = v_{\alpha\beta} - \hat{R}_s i_{\alpha\beta} + G(\hat{\lambda}_{\alpha\beta}^i - \hat{\lambda}_{\alpha\beta}) \quad (5)$$

where  $\hat{\lambda}_{\alpha\beta}$  is the estimated stator flux,  $G = g\mathbf{I}$  is a  $2 \times 2$  gain matrix,  $\hat{R}_s$  is the estimated stator resistance with error  $\tilde{R}_s = R_s - \hat{R}_s$  and  $\hat{\lambda}_{\alpha\beta}^i = e^{j\theta} \hat{\lambda}_{dq}^i$  is the LUTs-based current-model flux estimate with error  $\tilde{\lambda}_{dq}^i = \lambda_{dq} - \hat{\lambda}_{dq}^i$ . To aid in the analysis, the flux observer state equation (5) is transformed to the  $dq$  reference as

$$s\hat{\lambda}_{dq} = v_{dq} - \hat{R}_s i_{dq} - \omega \mathbf{J} \hat{\lambda}_{dq} + G(\hat{\lambda}_{dq}^i - \hat{\lambda}_{dq}). \quad (6)$$

The term hybrid indicates that for the electrical speeds below  $g$  rad/s, the current-model flux linkage  $\hat{\lambda}_{dq}^i$  prevails while voltage-model flux linkage  $\lambda_{dq}$  for the speeds above. Please note that the initial LUTs consist of the self-saturation curves only, whereas the cross saturation part will be populated using flux adaptation as described in the following. As said, the superscript  $\hat{\cdot}$  refers to the fact that the LUTs are under determination.

#### B. Projection Vector Framework

The general error signal  $\epsilon$  is defined as the projection of the difference in observed and current-model flux estimates on a projection vector  $\phi$  [15], expressed as

$$\epsilon = \phi^T (\hat{\lambda}_{dq} - \hat{\lambda}_{dq}^i). \quad (7)$$

It follows from (6) that the error signal  $\epsilon$  in terms of the current-model flux error  $\tilde{\lambda}_{dq}^i$  and the stator resistance error  $\tilde{R}_s$  is given by

$$\epsilon = \phi^T (s\mathbf{I} + G + \omega \mathbf{J})^{-1} \cdot \left( (s\mathbf{I} + \omega \mathbf{J}) \tilde{\lambda}_{dq}^i + \tilde{R}_s i_{dq} \right) \quad (8)$$

When applied to sensorless control [15], [16], the error signal (8) includes a rotor position error term that is zero here. To

aid in the design of projection vector in the following sections, the dc-component of the error signal (8) is considered:

$$\epsilon|_{s=0} = \phi^T (\mathbf{G} + \omega \mathbf{J})^{-1} \cdot \begin{bmatrix} -\omega \tilde{\lambda}_q^i + \tilde{R}_s i_d \\ +\omega \tilde{\lambda}_d^i + \tilde{R}_s i_q \end{bmatrix}. \quad (9)$$

Note that, due to the LF-PWM in  $q$ -axis, the terms  $i_q$  and  $\tilde{\lambda}_q^i$  in (9) are bipolar in nature. Considering that the flux-map LUTs contain the self-saturation curves only, the flux adaptation technique described in the following will be used to populate the cross-saturation current domain of the LUTs.

### C. Current-Model Flux Adaptation

Let  $\epsilon_d$  and  $\epsilon_q$  denote the LUTs-based current-model flux error signals along the projection vectors  $\phi_d$  and  $\phi_q$  for  $d$  and  $q$ -axis, respectively, expressed as

$$\epsilon_{dq} = \begin{bmatrix} \epsilon_d \\ \epsilon_q \end{bmatrix} = [\phi_d \ \phi_q]^T (\hat{\lambda}_{dq} - \hat{\lambda}_{dq}^i). \quad (10)$$

1) *d-axis Adaptation*: Using (9) and considering the resistance error to be null, the dc-component of the  $d$ -axis error signal is designed to be equal to the parameter error as

$$\epsilon_d|_{s=0} = \tilde{\lambda}_d^i \Rightarrow \phi_d^T = \frac{1}{\omega} \begin{bmatrix} 0 & 1 \end{bmatrix} (\mathbf{G} + \mathbf{J}\omega) \quad (11)$$

The  $d$ -axis flux adaptation is formulated to reflect the cross-saturation effect on the self-saturation stator flux from test- $d$  as

$$\hat{\lambda}_d^i(i_d, i_q) = \hat{\Lambda}_d(i_d, 0) + \frac{k_\lambda}{s} \epsilon_d \quad (12)$$

where  $k_\lambda$  is the integral gain. The corresponding  $i_{dq}$  point of the  $\hat{\Lambda}_d$  LUTs is populated with the steady-state value of (12).

2) *q-axis Adaptation*: As both  $i_q$  and  $\lambda_q$  are bipolar and synchronous, the error signal  $\epsilon_q$  is designed to be compatible with the adaptation law by transforming the parameter error to the first-quadrant (motoring) as

$$\begin{aligned} \epsilon_q|_{s=0} &= \tilde{\lambda}_q^i \cdot \text{sgn}(i_q) \\ \Rightarrow \phi_q^T &= \frac{-1}{\omega} [\text{sgn}(i_q) \ 0] (\mathbf{G} + \mathbf{J}\omega). \end{aligned} \quad (13)$$

Accounting for the polarity, the adaptation law supplements the cross-saturation offset to the self-saturation stator flux from test- $q$  as

$$\hat{\lambda}_q^i(i_d, i_q) = \hat{\Lambda}_q(0, i_q) + \text{sgn}(i_q) \cdot \frac{k_\lambda}{s} \epsilon_q. \quad (14)$$

As before, the  $i_{dq}$  point of the  $\hat{\Lambda}_q$  LUTs is populated with the steady-state value of (14).

It is of interest to point out that the incremental inductance matrix  $\mathbf{L}_\theta$  (2) can be retrieved from the identified flux-map in real-time; as an example:

$$\hat{l}_d(i_{dq}) = \frac{\hat{\Lambda}_d(i_d + \delta i_d, i_q) - \hat{\Lambda}_d(i_d, i_q)}{\delta i_d} \quad (15)$$

where  $\delta i_d$  is a small value (0.1 A). The other incremental inductances are computed in a similar fashion. They are crucial in tuning the CVC current regulators, model-predictive-control, and are indispensable in low-speeds sensorless control techniques.

3) *Stator Resistance Sensitivity*: Under inaccurate resistance, the error signals  $\epsilon_d$  and  $\epsilon_q$  are accompanied by the resistance error term as

$$\epsilon_d|_{s=0} = \tilde{\lambda}_d^i + \frac{\tilde{R}_s}{\omega} i_q \quad (16a)$$

$$\epsilon_q|_{s=0} = \text{sgn}(i_q) \cdot \tilde{\lambda}_q^i - \frac{\tilde{R}_s}{\omega} \text{sgn}(i_q) \cdot i_d. \quad (16b)$$

It can be discerned that the resistance error bearing terms,  $i_q$  in (16a) and  $\text{sgn}(i_q) \cdot i_d$  in (16b), are bipolar in nature at the frequency  $f_q$ . If the adaptation bandwidth is set to less than one third of the LF-PWM frequency, i.e.,  $k_\lambda < 0.33 \cdot 2\pi f_q$ , the bipolar resistance error terms can be largely filtered out. Therefore, the flux adaptation can be quasi-independent of resistance error. A dedicated experimental test is presented.

### D. Stator Resistance Adaptation

1) *Equivalent Stator Resistance Definition*: Accurate dc-link voltage measurement is assumed. Two potential sources of voltage error are considered: (i) discrepancy in temperature-dependent stator resistance estimate; (ii) non-ideal dead-time compensation of the inverter. If  $\hat{R}_s$  is the resistance used in the control,  $v_{dc}$  is the dc-link voltage,  $f_s$  is the switching frequency and  $\tilde{t}_d = t_d - \hat{t}_d$  is the error in the compensated dead-time, the voltage error can be expressed as [18], [19]

$$\tilde{v}_{\alpha\beta} = (R_s - \hat{R}_s) \mathbf{i}_{\alpha\beta} + \frac{4}{3} v_{dc} f_s \tilde{t}_d \text{sgn}(\mathbf{i}_{abc}) \quad (17)$$

where the nonlinear term  $\text{sgn}(\mathbf{i}_{abc})$  is a signum function of the inverter load current vector, defined as

$$\text{sgn}(\mathbf{i}_{abc}) = \frac{1}{2} \left( \text{sgn}(i_a) + e^{\mathbf{J} \frac{2\pi}{3}} \cdot \text{sgn}(i_b) + e^{\mathbf{J} \frac{4\pi}{3}} \cdot \text{sgn}(i_c) \right) \quad (18)$$

where  $\mathbf{i}_{abc}$  is the motor current vector expressed in phase components  $abc$ . The  $\text{sgn}(\mathbf{i}_{abc})$  vector is a unity vector along one of the six active discrete voltage vectors of a 2-level inverter that is closest to the current vector in the stationary  $\alpha\beta$  reference frame. The voltage error related to on-state voltage drop of power devices is included in the dead-time effect and the related compensation.

The fundamental component of the voltage error (17) is considered as the harmonic terms are inherently filtered out. The fundamental component due to the non-compensated dead-time voltage error is in phase with the current vector, just as the voltage error due to the inaccurate stator resistance. Hence, for modeling simplicity, an equivalent stator resistance error is defined from the fundamental component of (17) using Fourier series to include and compensate for both sources of error:

$$\tilde{R}_s = (R_s - \hat{R}_s) + \frac{1}{|\mathbf{i}_{dq}|} \frac{4}{\pi} v_{dc} f_s \tilde{t}_d. \quad (19)$$

Note that though the parasitic capacitance introduces harmonics in the applied voltage, it has been overlooked since they only marginally affect the fundamental voltage.



Fig. 9. Experimental Setup of 1.1 kW SyR and 11 kW PM-SyR motors under test on a dSPACE DS1103 control platform.

2) *Adaptation Law*: It is worth pointing out that, in addition to the two projection vectors (11) and (13), a third projection vector for stator resistance adaptation is feasible within the 2-D error domain ( $dq$ ) because the bipolar excitation provides the additional degree of freedom.

Let  $\epsilon_r$  denote the resistance error signal. Assuming null flux errors, the resistance error projection vector  $\phi_r$  is designed using (9) such that the dc-component of the error signal is equal to the resistance error as

$$\epsilon_r|_{s=0} = \tilde{R}_s \Rightarrow \phi_r^T = \frac{\dot{i}_{dq}^T}{|\dot{i}_{dq}|^2} (G + J\omega). \quad (20)$$

The resistance adaptation law is expressed as

$$\hat{R}_s = \frac{k_r}{s} \epsilon_r \quad (21)$$

where  $k_r$  is the integral gain.

3) *Current-Model Flux Sensitivity*: The influence of the current-model flux parameter errors on resistance adaptation is evaluated as

$$\epsilon_r|_{s=0} = \tilde{R}_s + \frac{\omega}{|\dot{i}_{dq}|^2} (\tilde{\lambda}_d^i i_q - \tilde{\lambda}_q^i i_d) \quad (22)$$

where the flux error terms are both bipolar in nature. As discussed before, a suitable selection of gain to filter out the bipolar signal is  $k_r < 0.33 \cdot 2\pi f_q$  and helps decoupling of the resistance adaptation from the current-model flux errors.

#### IV. EXPERIMENTAL RESULTS

The proposed scheme is validated experimentally on a 1.1 kW SyR and a 11 kW PM-SyR motors on a dSPACE DS1103 control platform running at a sampling frequency of 10 kHz. A picture of the setup is shown in Fig. 9. The parameters of

TABLE I  
MOTOR AND INVERTER PARAMETERS

Parameters	Symbol	SyR	PM-SyR	Units
Rated power	$P_n$	1.1	11	kW
Rated speed	$\omega_n$	1500	2500	rpm
Rated current	$I_n$	2.3	15.5	A
Rated torque	$T_n$	7.1	19	Nm
PM open-circuit flux	$\lambda_m$	-	0.12	Vs
DC link voltage	$V_{dc}$	565	565	V
Pole pairs	$p$	2	2	-
Stator resistance	$R_s$	5.9	0.4	$\Omega$
Motor inertia	$J$	0.0045	0.010	kgm <sup>2</sup>
Nominal dead-time	$t_d$	1.9	1.9	$\mu$ s
Switching frequency	$f_s$	10	10	kHz

the SyR and the PM-SyR motors under test are tabulated in Table I.

The speed controller bandwidth is set to  $2\pi \cdot 1$  rad/s. The flux observer gain is  $g = 2\pi \cdot 10$  rad/s. The adaptation gains are  $k_\lambda = 2\pi \cdot 2.5$  rad/s and  $k_r = 2\pi \cdot 0.5$  rad/s. The optimal speed-span for online adaptation is  $0.33 < \omega < 0.66$  p.u. and the LF-PWM frequency is set to  $f_q = 15$  Hz.

#### A. Systematic MMI with Current-Model Flux Adaptation

Following the hysteresis controlled self-saturation identification, the control systematically traverses the  $dq$  current plane for the cross-saturation identification. A minimum torque for speed regulation at free-shaft necessitates a minimum current on both  $d$  and  $q$ -axes for a SyR machine or just the  $q$ -axis for machines with magnets in the  $d$ -axis. The maximum current is determined by the inverter limits, subject to the voltage constraint at the maximum speed. For the reported tests, a  $10 \times 10$  grid with 100 data-points from  $i_{dq,min}^*$  to  $i_{dq,max}^*$  is considered. For each set of the references, a small time is elapsed ( $\approx 2$  s) to allow the dynamics of the adaptation to settle down to a steady-state before data acquisition. The total elapsed time per data-point is about 3.5 s and for the complete cross-saturation identification test is around six minutes.

1) *SyR Motor*: A minimum of  $i_{d,min}^* = |i_{q,min}^*| = 0.5$  A (0.15 p.u.) is set and a 50% overload is found achievable, i.e.,  $i_{d,max}^* = |i_{q,max}^*| = 5$  A (1.5 p.u.). As formerly discussed, the online adaptation is enabled only in the optimal speed-span for speeds greater than 500 rpm. Fig. 10(a) juxtaposes the identified flux curves against the reference curves that shows good correlation. The current-model flux error contours of  $d$  and  $q$ -axis are shown in Fig. 10(b) and 10(c), respectively. The maximum error is observed to be 0.009 Vs which is less than  $< 0.9\%$  of the rated flux.

2) *PM-SyR Motor*: A minimum current of  $|i_{q,min}^*| = 3$  A (0.13 p.u.) and a maximum current of  $i_{d,max}^* = |i_{q,max}^*| = 30$  A (1.34 p.u.) are chosen. The adaptation is active in speed-span  $833.3 < \omega_r < 1500$  rpm. Fig. 11(a) juxtaposes the identified flux curves against the reference curves that shows good correlation. The current-model flux error contours of  $d$  and  $q$ -axis are shown in Fig. 11(b) and 11(c), respectively, where the maximum error is observed to be 0.005 Vs.



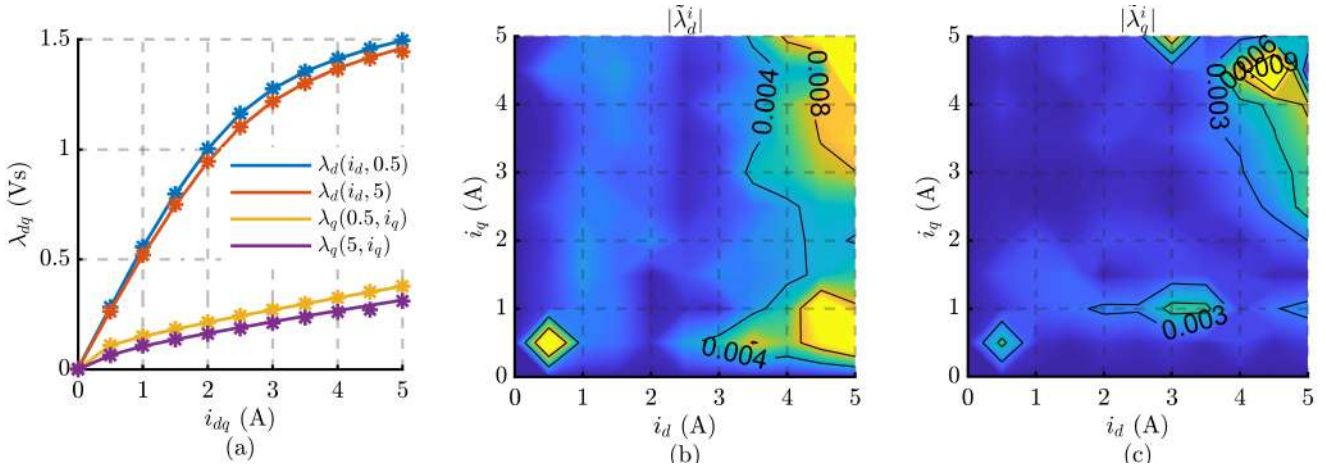


Fig. 10. SyR motor experimental MMI with self and cross-saturation: (a) Identified points (star) shown against reference flux-map (continuous line) showing good correlation; (b) Error contour in  $d$ -axis in Vs; (c) Error contour in  $q$ -axis in Vs.

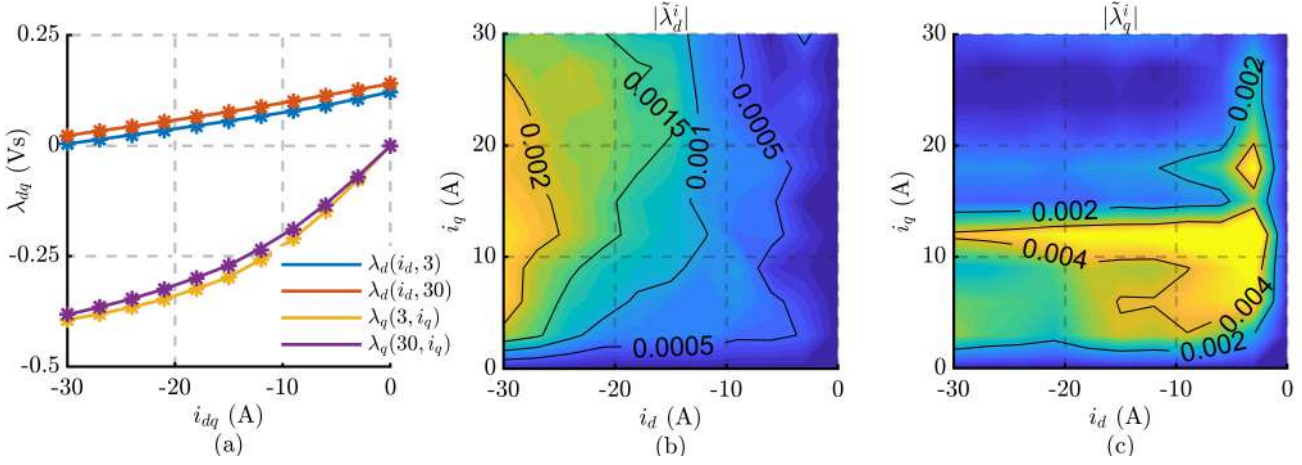


Fig. 11. PM-SyR motor experimental MMI with self and cross-saturation: (a) Identified points (star) shown against reference flux-map (continuous line) showing good correlation, where negative range of  $i_q$  is considered for space reasons; (b) Error contour in  $d$ -axis in Vs; (c) Error contour in  $q$ -axis in Vs.

### B. Stator Resistance Adaptation

1) *SyR Motor*: The stator resistance adaption is concurrently active along with the stator flux adaptation. Fig. 12(a) shows the contour plot of the estimated equivalent resistance accounting for non-idealities in the dead-time compensation as per (19). The characterization of the stator resistance and the dead-time error is shown in Fig. 12(b) from which the stator resistance is evaluated to  $\hat{R}_s = 5.9 \Omega$  and the dead-time error to  $\tilde{t}_d = -0.3 \mu s$ .

2) *PM-SyR Motor*: The equivalent stator resistance contour of the adaptation is shown in Fig. 13(a) and is characterized in Fig. 13(b). The stator resistance is evaluated to  $\hat{R}_s = 0.46 \Omega$  and the dead-time error to  $\tilde{t}_d = -0.1 \mu s$ . The discrepancy in dead-time evaluation between the two tests is attributed to the small magnitude of the voltage error ( $< 0.2\%$  of the DC-link voltage).

### C. Mechanical Inertia Identification

Exploiting the kinetic-rotor property of the proposed technique, the mechanical inertia can also be estimated without additional tests. The electrical steady-state data-points in

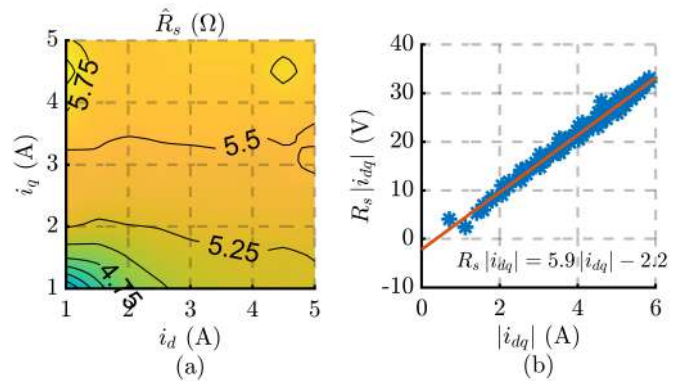


Fig. 12. SyR motor stator resistance adaptation: (a) Effective estimated resistance contour; (b) Characterization evaluating resistance and inverter dead-time.

Figs. 6 & 7 are selected that meet the criteria  $|i_q^* - i_q| < \delta i$ , where  $\delta i$  is a small value (0.1 A). For this refined dataset, the mean values of torque and acceleration are computed; it is recommended to low-pass-filter the acceleration at 50

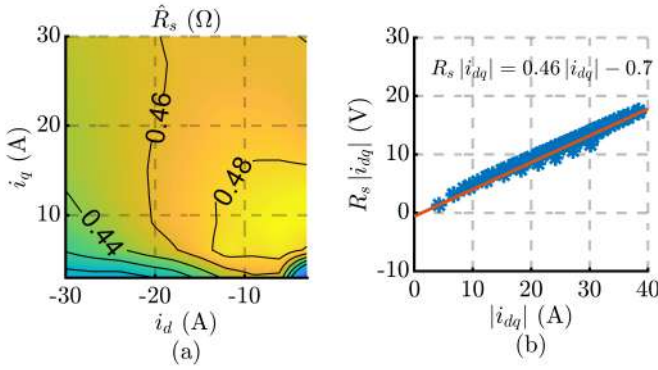


Fig. 13. PM-SyR motor stator resistance adaptation: (a) Effective estimated resistance contour; (b) Characterization evaluating resistance and inverter dead-time.

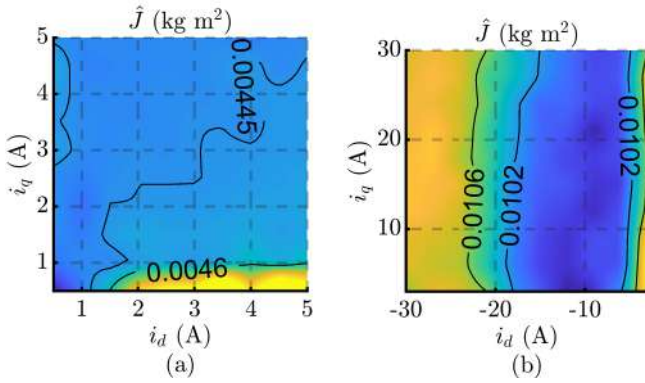


Fig. 14. Mechanical inertia identification from the kinetic-rotor cross-saturation tests: (a) SyR motor; (b) PM-SyR motor.

Hz to remove high-frequency noise (eg. incremental encoder discretization). Finally, the inertia is estimated from the ratio of the mean torque to the mean acceleration; the contours of SyR and PM-SyR motors are shown in Figs. 14(a) & 14(b), respectively. The results are accurate up to three decimal places, in accordance with the expected values  $J = 0.0045$  kg m<sup>2</sup> for the SyR and  $J = 0.010$  kg m<sup>2</sup> for the PM-SyR machines. A small variation in the fourth decimal place is observed; the inertia estimates of the high-torque and large speed-swing data-points are expected to be more reliable.

#### D. Dynamics of Current-Model Flux Adaptation

The time-plots of the current-model flux adaptation of PM-SyR motor is shown in Fig. 15 for the set-points  $i_d^* = -22$  A (1.0 p.u.) and  $|i_q^*| = 22$  A (1.0 p.u.). The speed-swing for these reference points is observed to be approximately 1000 rpm although the adaptation, if enabled, is only active for speeds greater than 0.33 p.u.,  $\omega_r > 833.3$  rpm.

The adaptation is enabled at  $t = 0$  s. For the time  $t < 0$  s, the current-model flux estimates are derived from the self-saturation identification of test- $d$  and test- $q$ , and hence, an error of  $|\tilde{\lambda}_d^i| = 0.014$  Vs and  $|\tilde{\lambda}_q^i| = 0.018$  Vs exists due to the cross-saturation effect. Once the adaptation is enabled at  $t > 0$  s, the errors are mitigated and the settling time is observed to be around 0.2 s.

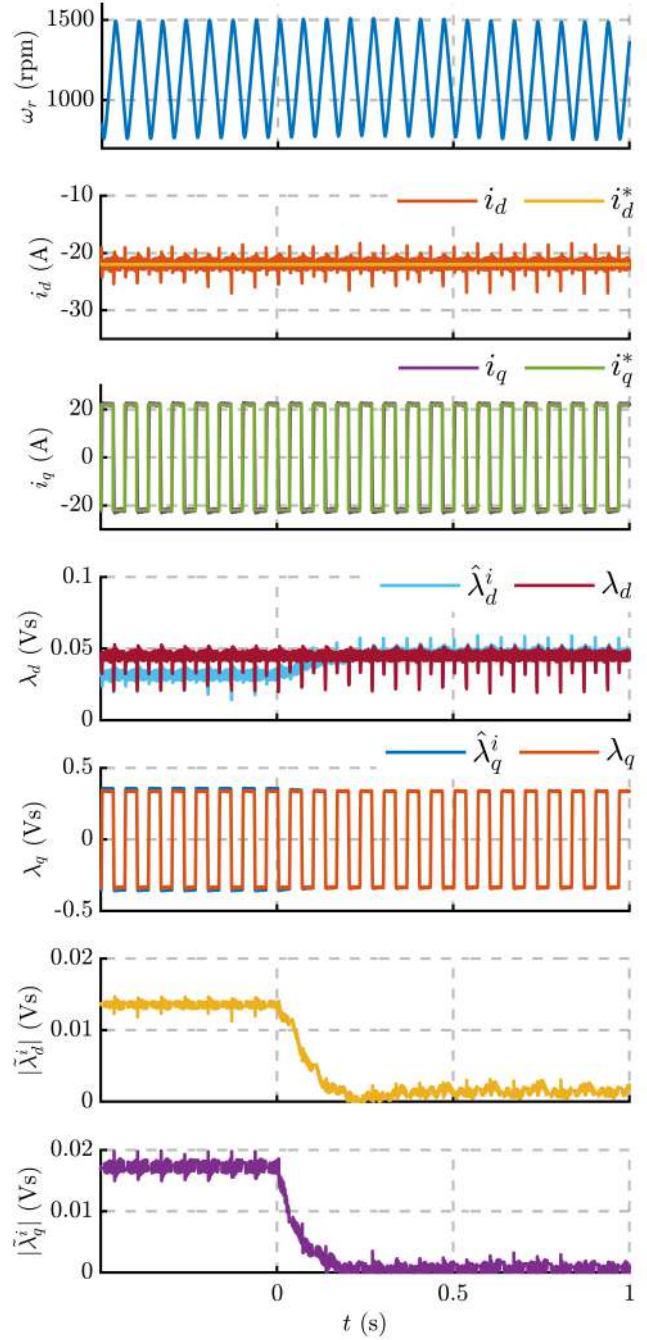


Fig. 15. PM-SyR motor time plots to illustrate the dynamics of current-model flux adaptation at  $i_d^* = -22$  A (1.0 p.u.) and  $|i_q^*| = 22$  A (1.0 p.u.). The adaptation is enabled at  $t = 0$  s.

#### E. Dynamics of Stator Resistance Adaptation

The dynamics of the stator resistance adaptation of PM-SyR motor at the reference set-points  $i_d^* = -22$  A (1.0 p.u.) and  $|i_q^*| = 22$  A (1.0 p.u.) is shown in Fig. 16. A step change in the compensated dead-time  $\hat{t}_d \rightarrow 3.9 \mu\text{s}$  is imposed at time  $t = 0$  s which introduces an error  $\hat{t}_d = -1 \mu\text{s}$ .

As the adaptation is active, the initial resistance error in the time  $t < 0$  s is considered zero, i.e.,  $\hat{R}_s(t < 0) = R_s = 0.46 \Omega$ . Then, it follows from (19) that the equivalent resistance error at  $t = 0$  s due to the dead-time error  $\hat{t}_d = -1 \mu\text{s}$



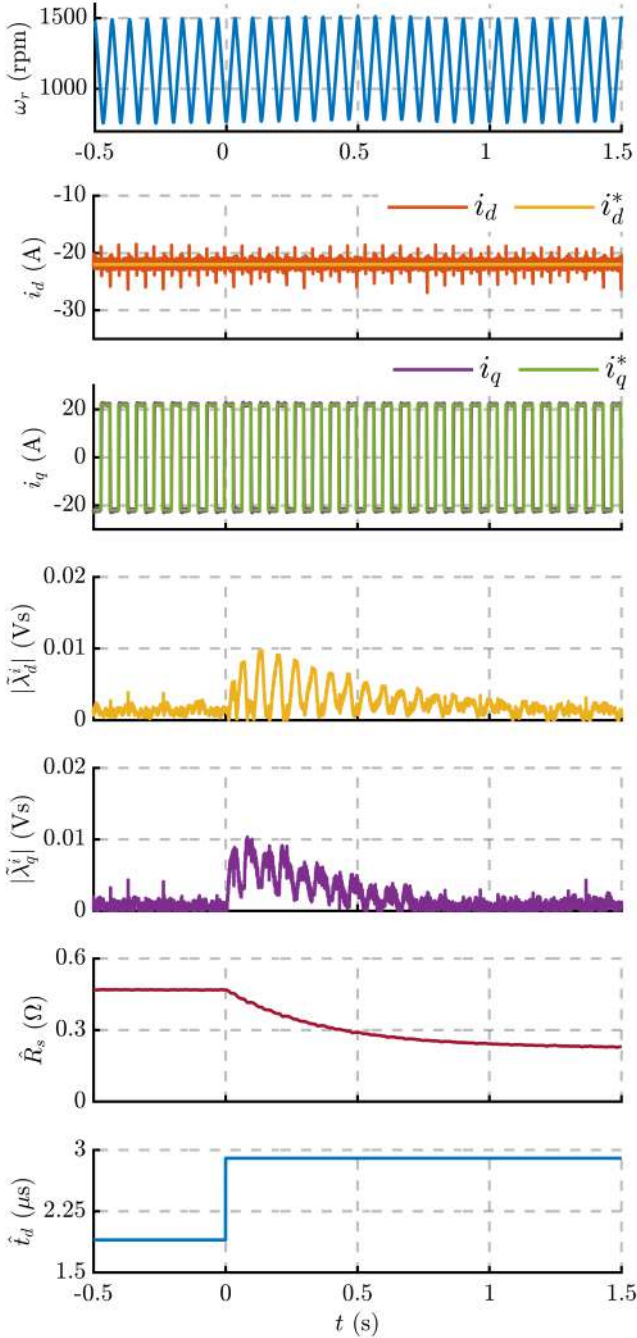


Fig. 16. PM-SyR motor time plots to illustrate the dynamics of stator resistance adaptation at  $i_d^* = -22$  A (1.0 p.u.) and  $i_q^* = 22$  A (1.0 p.u.); an error in dead-time  $\hat{t}_d = -1\mu\text{s}$  is introduced at  $t = 0$  s.

is  $\hat{R}_s = -0.23\Omega$ . With a settling time of 1.2 s, the estimated resistance converges to  $\hat{R}_s = R_s + \hat{R}_s = 0.23\Omega$ . Despite the current-model flux adaptation gains tuned to minimize the resistance sensitivity, small disturbances are observed in the flux error which is mitigated once the resistance estimation attains steady-state.

## V. CONCLUSION

A self-commissioning technique for magnetic-model-identification at free-shaft that is applicable to the family of

synchronous machines is proposed. A novel LF-PWM scheme for speed regulation via bipolar  $i_q$  is developed for kinetic-rotor cross-saturation identification. The operating points on the zero-torque locus are identified at standstill condition using a hysteresis current controller with square-wave voltage injection.

The cross-saturation domain of the flux-map LUTs is populated online using a projection-vector based stator flux adaptation scheme mutated from sensorless control techniques.. Moreover, an additional projection vector is used to compensate for the stator resistance and inverter dead time voltage errors. The gains of the adaptation law are tuned such that the coupling between stator fluxes and resistance is minimal.

The proposed scheme is experimentally validated on a 1.1 kW SyR and a 11 kW PM-SyR motor test-bench. The identified flux-map shows good correlation with the reference maps and the maximum error is less than  $< 1\%$  of the rated flux, producing negligible error in the interpretation of optimal operation with MTPA and MTPV laws.

## REFERENCES

- [1] H. A. A. Awan, Z. Song, S. E. Saarakkala, and M. Hinkkanen, "Optimal Torque Control of Saturated Synchronous Motors: Plug-and-Play Method," *IEEE Transactions on Industry Applications*, p. 1, 2018.
- [2] G. Pellegrino, R. I. Bojoi, and P. Guglielmi, "Unified direct-flux vector control for AC motor drives," *IEEE Transactions on Industry Applications*, vol. 47, no. 5, pp. 2093–2102, 2011.
- [3] IEEE, "IEEE Trial-Use Guide for Testing Permanent Magnet Machines," pp. 1–56, 2015.
- [4] E. Armando, R. I. Bojoi, P. Guglielmi, G. Pellegrino, and M. Pastorelli, "Experimental identification of the magnetic model of synchronous machines," *IEEE Transactions on Industry Applications*, vol. 49, no. 5, pp. 2116–2125, 2013.
- [5] S. A. Odhano, R. Bojoi, t. G. Roşu, and A. Tenconi, "Identification of the Magnetic Model of Permanent-Magnet Synchronous Machines Using DC-Biased Low-Frequency AC Signal Injection," *IEEE Transactions on Industry Applications*, vol. 51, no. 4, pp. 3208–3215, 2015.
- [6] L. Peretti, P. Sandulescu, and G. Zanuso, "Self-commissioning of flux linkage curves of synchronous reluctance machines in quasi-standstill condition," *IET Electric Power Applications*, vol. 9, no. 9, pp. 642–651, 2015.
- [7] G. Pellegrino, B. Boazzo, and T. M. Jahns, "Magnetic Model Self-Identification for PM Synchronous Machine Drives," *IEEE Transactions on Industry Applications*, vol. 51, no. 3, pp. 2246–2254, 2015.
- [8] K. Liu, J. Feng, S. Guo, L. Xiao, and Z. Zhu, "Identification of Flux Linkage Map of Permanent Magnet Synchronous Machines Under Uncertain Circuit Resistance and Inverter Nonlinearity," *IEEE Transactions on Industrial Informatics*, vol. 14, no. 2, pp. 556–568, 2018.
- [9] N. Bedetti, S. Calligaro, and R. Petrella, "Stand-Still Self-Identification of Flux Characteristics for Synchronous Reluctance Machines Using Novel Saturation Approximating Function and Multiple Linear Regression," *IEEE Transactions on Industry Applications*, vol. 52, no. 4, pp. 3083–3092, 2016.
- [10] S. Wiedemann and R. M. Kennel, "Encoderless self-commissioning and identification of synchronous reluctance machines at standstill," in *IEEE International Symposium on Industrial Electronics*, 2017, pp. 296–302.
- [11] M. Hinkkanen, P. Pescetto, E. Mölsä, S. E. Saarakkala, G. Pellegrino, and R. Bojoi, "Sensorless Self-Commissioning of Synchronous Reluctance Motors at Standstill Without Rotor Locking," *IEEE Transactions on Industry Applications*, vol. 53, no. 3, pp. 2120–2129, 2017.
- [12] P. Pescetto and G. Pellegrino, "Automatic Tuning for Sensorless Commissioning of Synchronous Reluctance Machines Augmented with High-Frequency Voltage Injection," *IEEE Transactions on Industry Applications*, vol. 54, no. 5, pp. 4485–4493, 2018.
- [13] A. Varatharajan, P. Pescetto, and G. Pellegrino, "Sensorless Self-Commissioning of Synchronous Reluctance Machine with Rotor Self-Locking Mechanism," in *2019 IEEE Energy Conversion Congress and Exposition (ECCE)*, 2019, pp. 812–817.

- [14] S. A. Odhano, P. Pescetto, H. A. A. Awan, M. Hinkkanen, G. Pellegrino, and R. Bojoi, "Parameter Identification and Self-Commissioning in AC Motor Drives: A Technology Status Review," *IEEE Transactions on Power Electronics*, vol. 34, no. 4, pp. 3603–3614, 2019.
- [15] M. Hinkkanen, S. E. Saarakkala, H. A. A. Awan, E. Mölsä, and T. Tuovinen, "Observers for Sensorless Synchronous Motor Drives: Framework for Design and Analysis," *IEEE Transactions on Industry Applications*, vol. 54, no. 6, pp. 6090–6100, 2018.
- [16] A. Varatharajan and G. Pellegrino, "Sensorless Synchronous Reluctance Motor Drives: A General Adaptive Projection Vector Approach for Position Estimation," *IEEE Transactions on Industry Applications*, vol. 56, no. 2, pp. 1495–1504, 2020.
- [17] A. Varatharajan, G. Pellegrino, and E. Armando, "Self-Commissioning of Synchronous Reluctance Motor Drives: Magnetic Model Identification with Online Adaptation," in *2020 IEEE Energy Conversion Congress and Exposition (ECCE)*, 2020, pp. 5353–5360.
- [18] G. Pellegrino, P. Guglielmi, E. Armando, and R. I. Bojoi, "Self-commissioning algorithm for inverter nonlinearity compensation in sensorless induction motor drives," *IEEE Transactions on Industry Applications*, vol. 46, no. 4, pp. 1416–1424, 2010.
- [19] I. R. Bojoi, E. Armando, G. Pellegrino, and S. G. Rosu, "Self-commissioning of inverter nonlinear effects in AC drives," *2012 IEEE International Energy Conference and Exhibition, ENERGYCON 2012*, pp. 213–218, 2012.